Redox Biology 37 (2020) 101690

Contents lists available at ScienceDirect

Redox Biology

journal homepage: www.elsevier.com/locate/redox

Research Paper

Galuminox: Preclinical validation of a novel PET tracer for non-invasive imaging of oxidative stress *in vivo*

Jothilingam Sivapackiam [a], Fuyi Liao [b], Dequan Zhou [b], Kooresh I. Shoghi [a,d], Robert J. Gropler [a,d], Andrew E. Gelman [b], Vijay Sharma [a,c,d,*]

[a] Mallinckrodt Institute of Radiology, USA
[b] Departments of Surgery, Pathology and Immunology, Washington University School of Medicine, St. Louis, MO, 63110, USA
[c] Department of Neurology, Washington University School of Medicine, St. Louis, MO, 63110, USA
[d] Department of Biomedical Engineering, School of Engineering & Applied Science, Washington University, St. Louis, 63105, USA

ARTICLE INFO

Keywords:
Galuminox
Acute lung injury
Oxidative stress
PET imaging

ABSTRACT

Overproduction of reactive oxygen species (ROS) is a well-established indicator of ongoing tissue inflammation. However, there is a scarcity of molecular imaging probes capable of providing noninvasive sensitive detection of ROS for allowing longitudinal studies of disease pathology and/or monitoring therapeutic efficacy of ROS scavengers. Herein, we report synthesis and chemical characterization of a novel metalloprobe, Galuminox, a moderately fluorescent agent that detects superoxide and hydrogen peroxide generation. Using live-cell fluorescence imaging analysis, Galuminox demonstrates ability to detect superoxide and monitor effects of ROS-attenuating agents, such as Carvedilol, Dexrazoxane, and mitoTempo in lung epithelial A549 cells. Furthermore, LPS stimulation of A549 cells that either express the mitochondria targeted fluorescent protein Keima or are stained with MitoSOX, a mitochondria-specific superoxide probe, indicates preferential co-localization of Galuminox with mitochondria producing elevated amounts of superoxide. Dynamic PET/CT scans 45 min post tail-vein administration of ^{68}Ga-Galuminox show 4-fold higher uptake and stable retention in lungs of LPS treated mice compared to their saline-only treated counterparts. Post preclinical PET imaging, quantitative biodistribution studies also correlate with 4-fold higher retention of the radiotracer in lungs of LPS treated mice compared with their saline-only treated control counterparts. Consistent with these observations, lung cells isolated from LPS-treated mice demonstrated elevated ROS production deploying CellROX, the ROS probe. Finally, Galuminox uptake correlates with histological and physiological evidence of acute lung injury as evident by polynuclear infiltration, thickening of the alveolar epithelial membranes and increased bronchioalveolar lavage protein content. Taken collectively, these data indicate that ^{68}Ga-Galuminox tracer uptake is a measure of ROS activity in acutely injured lungs and suggests its potential utility in monitoring oxidative stress in other diseases.

1. Introduction

Reactive oxygen species (ROS) regulate critical physiological functions, including cellular homeostasis, vascular diameter [1], oxygen sensing [2], host pathogen defense [3], skeleton muscle physiology [4], gene transcription, and signal transduction [5]. Additionally, ROS are by-products of enzymatic reactions in various cell compartments, including the cytoplasm, cell membrane, endoplasmic reticulum (ER), and mitochondria [6]. The homeostatic balance via redox regulation of ROS is required to prevent a pro-oxidative cellular state; the biochemical phenomenon commonly known as "oxidative stress." During oxidative stress, the continuous production of ROS exceeds the ability of the native antioxidative defense system to mitigate/neutralize free radicals and their byproducts, thus inducing damage to DNA, proteins and lipids [7–9]. Noticeably, this imbalance in production/mitigation of ROS has been implicated in the pathogenesis of numerous diseases, such as cardiovascular disease [10], diabetes [11], atherosclerosis [12], asthma [13], Alzheimer's disease [14], psoriasis [15], rheumatoid arthritis

* Corresponding author. Mallinckrodt Institute of Radiology Washington University School of Medicine, Box 8225 510 S. Kingshighway Blvd, St. Louis, MO, 63110, USA.
E-mail address: sharmav@wustl.edu (V. Sharma).

https://doi.org/10.1016/j.redox.2020.101690
Received 26 May 2020; Received in revised form 14 August 2020; Accepted 16 August 2020
Available online 21 August 2020

[16], aging [17], and acute lung injury (ALI) [18,19].

Currently, ALI, clinically characterized as acute respiratory distress syndrome (ARDS), is assessed by a combination of pathophysiological and functional indicators including diffuse alveolar damage, hypoxemia, and pulmonary edema [20,21]. In developed countries, ALI is the predominant cause of intensive care unit deaths. Notably, there is a lack of diagnostic technology that detects ALI. Routine laboratory tests are normally nonspecific and indicate organ injury reflective of severe hypoxemia or associated shock and systemic inflammation. Furthermore, imaging findings are also variable and depend upon the severity of the disease. Expectedly, initial chest radiographs typically show bilateral diffuse alveolar opacities with dependent atelectasis [22]. Similarly, computed tomography (CT) of the chest has been shown to indicate a widespread patchy and/or coalescent airspace opacities that are usually more apparent in the dependent lung zones [23–25]. Finally, while bedside lung ultrasound continues to remain investigational, preliminary clinical studies do suggest approximately 80% sensitivity for the diagnosis of ARDS compared with CT chest [26]. Therefore, new molecularly specific diagnostic agents capable of imaging noninvasively an acute lung injury have been sought.

For designing molecular imaging agents to monitor oxidative stress, major ROS sensing probes (reported to date) have been conceptualized based upon their fluorescence and chemiluminescence traits [27–33]. Although immensely beneficial mechanistic information has been gained from these preclinical studies, agents capable of measuring ROS levels for translational imaging are desired. For interrogating role of ROS in mediating pathophysiology of disease states, PET tracers provide desired high sensitivity and quantifiable readout to enable deep tissue imaging, while also assisting in evaluating efficacy of therapeutic regimens. Consequently, significant efforts have been made worldwide for designing and validating ROS sensing radiotracers.

For conceptualizing radiotracers, ROS-sensitive fluorescent probes such as DHE (dihydroethidium), mitoSOX, and 5-(and 6)-chloromethyl-2′,7′-dichlorohydrofluorescein diacetate (CM-H_2DCFDA) offer interesting template scaffolds (Fig. 1). Therefore, it is not surprising that the design of first-generation ROS tracers consists of the DHE motif within their molecular scaffolds due to its ability to detect superoxide anion. Taking advantage of molecular targeting traits of DHE, while 6-(4-((1-(2-[^{18}F]-fluoroethyl)-1H-1,2,3-triazol-4-yl)methoxy)phenyl)-5-methyl-5,6-dihydrophenanthridine-3,8-diamine (^{18}F-FDMT) and 6-[4-(2-[^{18}F]-fluoroethoxy)phenyl]-5-methyl-5,6-dihydrophenanthridine-3,8-diamine (^{18}F-DHMT) have been investigated for anthracycline-induced cardiotoxicity (Fig. 1) in vivo [34,35], another tracer ^{11}C-hydromethidine has been studied for ROS activity within the brain [36]. Furthermore, another novel tracer comprising hydrogen peroxide sensitive boronic ester precursor of 3′-deoxy3’-[^{18}F]-fluorothymidine (^{18}F-FLT) has also been reported. The strategic design releases the FLT within cells, and is phosphorylated by thymidine kinase for trapping within the cells [37]. Finally, a hydrocyanine dye (IR780) analogue has been synthesized by substituting an ^{18}F-fluorinated prosthetic group to obtain a multimodality (PET/Optical) probe for allowing detection of superoxide and hydroxyl radicals [38]. Although promising strategy, the hydrophobic tracer shows substantial retention within the blood pool of normal rodents even after 2 h, a critical factor that can potentially negatively impact signal to background ratios desired for preclinical translational imaging [38]. Importantly, PET tracers capable of allowing noninvasive imaging of ROS mediated pathophysiology in ALI have not been developed. In context of ALI, there are very limited studies on rodent models focused upon ^{18}F-FDG, the main workhorse of PET imaging landscape in diagnostic nuclear medicine. Based upon a principle that ALI induces neutrophil activation, and metabolically active neutrophils consume more glucose per cell, thereby ALI insult would result in higher uptake of the ^{18}F-FDG. However, there are also limitations of these studies. For example, ^{3}H-deoxyglucose uptake correlates with glycogen synthesis and glycolysis and not necessarily with ROS production [39]. Neutrophils, have few mitochondria, produce the bulk of their ROS through NADPH Oxidase 2 [40] and are largely not dependent on oxidative phosphorylation that drives the bulk of superoxide production for most cells [41]. Additionally, deploying ^{3}H-deoxyglucose, micro-autoradiography studies do not show any alveolar macrophage signal in acutely inflamed lung tissue [42]. While strengths and weaknesses of PET FDG in ALI models have been continuously debated, to our knowledge, there are no PET-metalloprobes capable of allowing imaging of ROS mediated pathophysiology in vivo.

Among the chemiluminescent probes, luminol and its analogues have been widely studied for detecting ROS [43], as substrate for monitoring ROS using nonimmunoassay or immunoassays kits [44], and a forensic tool in the form of aerosols for detecting trace blood patterns at the crime scenes [45,46]. Luminol has been shown to detect mainly a superoxide in human neutrophils [47]. For designing a proof-of-concept PET tracer, we synthesized a variation on the theme by incorporating a glycine linker into luminol for a conjugation into a chelator core to enable incorporation of a radionuclide to assess potential of the radiotracer for investigating role of ROS in pathophysiology of diseases in

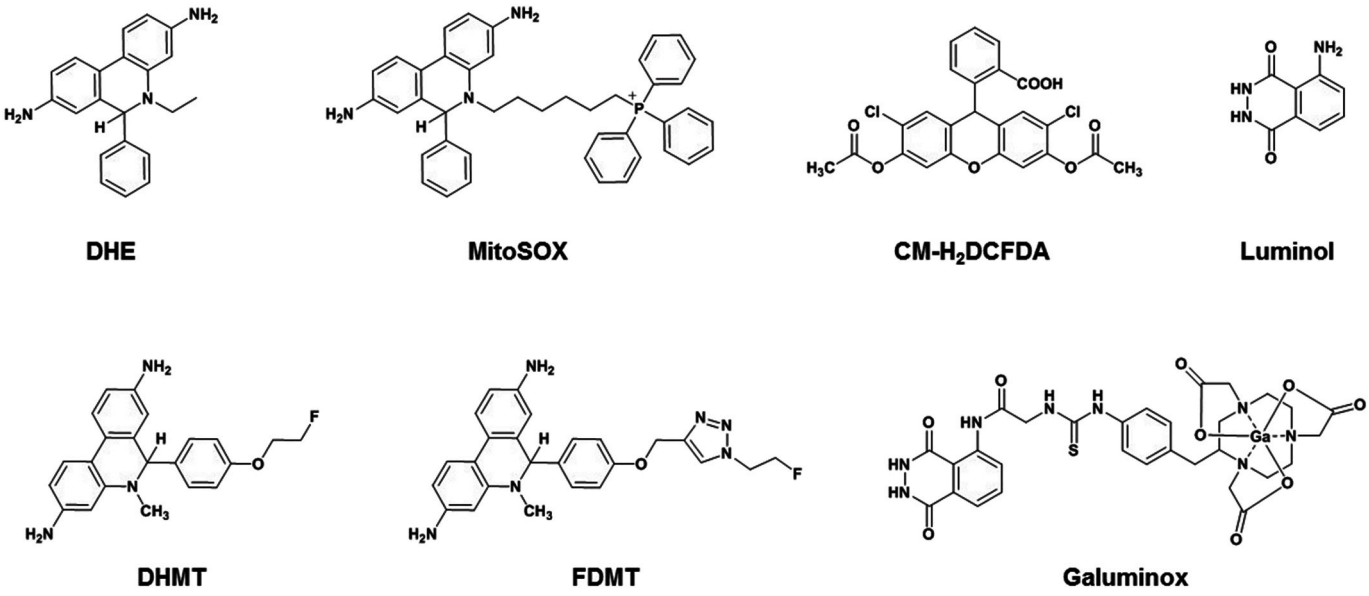

Fig. 1. Chemical structures of ROS probes.

vivo. To perform a functional imaging of oxidative stress-induced inflammation within the lungs, herein, we show ability of ^{68}Ga-Galuminox to detect ROS *in cellulo* using live-cell fluorescence imaging, and in vivo by deploying a well-validated endotoxemia model using Lipopolysaccharide (LPS), in the age-matched C57BL6 mice through PET/CT imaging, and correlate PET imaging data through ex vivo studies.

2. Methods

2.1. Chemistry reagents and general methods

All reagents were purchased from Sigma-Aldrich, unless otherwise stated. ^{1}H NMR was recorded on Bruker (400 MHz) spectrometer; chemical shifts are reported in δ (ppm) with reference to TMS. Mass analyses were performed using Agilent 1200 HPLC, 1956 MSD (column Shim-pack XR-ODS 30 mm × 3.0 mm, 2.2 μm) operating in ES (+) ionization mode. All HPLC analysis was performed with a Waters System 600 equipped with dual λ detector 2487 (set to 280 and 214 nm) and a γ-detector (Bioscan) for identification of radio-peaks. For radio-TLC analysis, silica gel plates were scanned using Bioscan 2000 system.

2.2. Chemical synthesis

2.2.1. Synthesis of precursor ligand (LG-NOTA)

Luminol-glycine (LG; 0.18 mmol) and *p*–SCN–Bn-NOTA (0.18 mmol) were dissolved in dimethylformamide (5 mL) and freshly distilled trimethylamine (100 μL) was added. The contents were mixed and stirred at 50 °C for 15 h. Following completion of the reaction, the precursor ligand was precipitated by addition of ethyl acetate, precipitates were filtered, washed with ethyl acetate (3 × 5 mL), followed by diethyl ether, and dried to obtain LG-NOTA (Yield: 105 mg; 0.15 mmol; 83.3%). ^{1}H NMR: (400 MHz, DMSO-d_6) δ: 13.17 (s, 1H), 10.38 (s, 1H), 8.90 (d, 1H), 8.61 (s, 1H), 7.91 (s, 1H), 7.59 (d, 1H), 7.49 (d, 2H), 7.17 (d, 2H), 4.25 (s, 2H), 3.60–2.60 (m, 19H); MS (ESI): Calcd. for $C_{30}H_{36}N_8O_9S$; 684.23; Found: 685.23.

2.1.2. Synthesis of Ga-LG-NOTA (Galuminox)

To obtain metalloprobe, the LG-NOTA (0.20 mmol) and $GaCl_3$ (0.20 mmol) were dissolved in dry DMSO (2 mL) and heated to 110 °C for 60 min. Following reaction, the product was precipitated by addition of EtOAc, filtered, washed with ethyl acetate, diethyl ether, and dried to obtain Ga-LG-NOTA (Yield: 126 mg; 0.17 mmol; 85%). ^{1}H NMR (400 MHz, DMSO-d6) δ: 13.11 (s, 1H), 11.86 (Br. s, 1H), 10.22 (s, 1H), 8.95 (d, 1H), 8.40 (s, 1H), 7.86 d, 1H), 7.63 (d, 1H), 7.52 (s, 2H), 7.23 (s, 2H), 4.32 (s, 2H), 3.64–2.91 (m, 19H); ^{1}H NMR: MS (ESI): Calcd for $C_{30}H_{33}GaN_8O_9S$; 750.7; Found $(M + K)^+$: 789.7.

2.3. Radiochemistry

Radiolabeled ^{68}Ga-Galuminox was synthesized using a procedure described earlier with slight modifications [48]. Briefly, gallium-68 was eluted from a generator (IGG100-50 M) using 0.1 M HCl (1.1 mL), NaOAc buffer (pH 5, 400 μL) was added to the eluent mixture, the pH was adjusted to 4.5, mixed with a solution of the LG-NOTA ligand (50 μg, 50 μL) dissolved in a solution of 90% ethanol/10% polyethylene glycol 200, and heated at 100 °C for 15 min. The reaction was monitored using radio-TLC. Following completion of the reaction, the reaction mixture was passed through cation exchange column (Phenomenex; Strata-X-C 33 m Polymeric Strong Cation; 30 mg/mL) to remove trace metal impurities and unreacted gallium-68. Finally, ^{68}Ga-Galuminox was analyzed using radio-HPLC for purity on a C-18 reversed-phase column (Alltima, 3 μm, Rocket 53 × 7mm) using an eluent gradient of methanol with 0.1% (v/v) trifluoroacetic acid and water with 0.1% (v/v) trifluoroacetic acid (isocratic 20% methanol in water for 5 min; gradient from 20% to 90% methanol in water from 5 to 40 min, at a flow of 1 mL/min). ^{68}Ga-Galuminox eluted with a retention time of 7 min (radiochemical purity > 98% and radiochemical yield: 97% decay corrected (reference to gallium-68 measured at the start of the reaction)). Additionally, ^{68}Ga-Galuminox was also analyzed by radio-TLC (methanol (v/v 0.1% TFA)/water (v/v 0.1% TFA) in a ratio of 9:1 ($R_f = 0.53$) using silica gel plates. The radiotracer was characterized by spiking an unlabeled analytically characterized sample of Galuminox (10 μg) with the ^{68}Ga-Galuminox, using UV and radio-detectors. Finally, the purified radiolabeled fraction was diluted into sterile saline containing 2% ethanol (pH 7) and deployed for micro-PET imaging.

2.3.1. Detection of ROS using Galuminox in vitro fluorescence assay

All methodology for fluorescence assays is described in the supplementary information. Briefly, these assays were performed in phosphate buffer saline (PBS, 1x, pH 7.2). Reagents were prepared and stored at 4 °C. Catalytic enzymes were diluted using commercial buffers and stored as per manufacturer instructions. Final concentrations for Galuminox, glucose, glucose oxidase, xanthine, xanthine oxidase (XO), superoxide dismutase (SOD), catalase (CAT), Linsidomine (SIN-1 chloride), and 2,4-carboxyphenyl-4,4–5,5-tetramethyl-imidazoline-1-oxyl-3-oxide (CPTIO) are listed in Table S1. For fluorescence measurements, Galuminox was incubated with G-GOx/X-XO/SIN-1 either in absence or presence of SOD/CAT/CPTIO for 15 min at 37 °C. All measurements of fluorescence were performed in triplicates, using a Corning 96-well (12 columns × 8 rows) plate with a final volume of 200 μl per well. Data were collected using Varian Cary Eclipse Fluorescence Spectrophotometer (Plate reader), normalized to fluorescence of buffers without Galuminox, the fluorescence output was determined in arbitrary units, converted into % intensity, and plotted using Prism – GraphPad.

2.4. Bioassays

2.4.1. Cell culture

Human alveolar basal epithelial (A549) adenocarcinoma cells were grown in Dulbecco's Modified Eagle Medium (DMEM) supplemented with L-glutamine (2 mM), penicillin/streptomycin (200 I·U.) and heat-inactivated fetal calf serum (10%). The cells were grown at 37 °C under a 5% CO_2 atmosphere.

2.4.2. A549 cells expressing mt-Keima

mt-Keima has been described previously [49]. A modified mt-Keima cDNA was generated from the mt-Keima open reading frame encoded within pCHAC-mt-mKeima (Addgene, Waterman MA) by PCR amplification with primers that include an extra N-terminal MT-COX3 leader peptide to further enhance localization of Keima protein to mitochondria. The resulting mt-Keima cDNA PCR product was then subcloned into multiclonal site (5′Xba1, 3′ EcoR1) of the lentiviral vector backbone Ex-EGFP-LV105 (Genecopia, Rockville, MD), which results in the deactivation of EGFP expression to create Ex-mt-Keima. Thereafter, Ex-mt-Keima lentiviral vector was packaged into lentiviral particles (Genecopia) and transfected into A549 cells (ATCC, Manassas VA) at a 10 : 1 multiplicity of infection under puromycin selection (Sigma, St Louis MO) treatment at 2 μg/ml.

2.4.3. Fluorescence imaging studies

Live cell fluorescence imaging studies were performed at Washington University Center for Cellular Imaging (WUCCI). For imaging studies, A549 cells or their mt-Keima transfected counterparts were plated onto borosilicate 8-well chambered coverglass (Labtek) and allowed to grow to approximately 70% confluence at 37 °C under 5% CO_2 atmosphere in the culture media (200 μL) and treated with LPS (1 μg/mL) for 24 h. Following LPS treatments, all wells were rinsed with fresh media. For evaluating impact of ROS on uptake profiles of the metalloprobe, cells were first incubated with mitoSOX (0.5 μM) at 37 °C for 15 min, then wells were rinsed with PBS (3 × 200 μL), and fresh media (200 μL) was added, followed by incubation with either

Galuminox (20 μM) or media alone at 37 °C for 1 h, while maintaining continuous influx of 5% CO_2. However, for tracking of intracellular localization of the probe, following LPS treatments for 24 h, A549 cells were incubated simultaneously with either Galuminox (20 μM) and lysotracker Red (1 μM) or media alone at 37 °C for 1 h under continuous influx of 5% CO_2. Similarly, following treatments with LPS, mt-Keima transfected A549 cells were also incubated simultaneously with either Galuminox (20 μM) or media alone at 37 °C for 1 h under continuous influx of 5% CO_2. Cellular accumulation studies were performed by using an inverted Nikon A1Rsi laser scanning confocal microscope using either a 20× dry or 60× oil objective lens (Nikon Instruments Inc., NY, USA). 405, 514 and 640 nm lasers were used for the detection of Galuminox, MitoSOX and Lysotracker deep red, respectively. Throughout the data acquisition process, cells were maintained at 37 °C with 5% CO2, controlled by a Tokai Hit stage-top incubation system (Shizuoka, Japan). Acquisition was performed using Nikon NIS-Elements software (Nikon Instruments Inc., NY, USA.). Images were processed and analyzed using the ImageJ software package (NIH). Cellular uptake of Galuminox was then quantified (wherein corrected total cellular fluorescence (CTCF) = integrated density–(area of selected cell × mean fluorescence of background readings) [50,51] using protocols described elsewhere [52]. The quantitative analysis for colocalized fluorescence signal within the merged channel was performed using EzColocalization, an open source plugin to ImageJ that enables quantification of colocalized signals from 2 or more channels in microscopy images [53]. For analysis, ROIs were drawn on cells of both channels, scatter plots were obtained, and Pearson's Correlation Coefficients (PCC) were determined as described previously [54].

For evaluation of therapeutic effects of drugs, such as Carvedilol (CAR), Dexrazoxane (DEX), and mitoTempo (MT) on either serum/glucose deprived media- or LPS-induced superoxide production, A549 cells were incubated with either LPS (1 μg/mL) or serum/glucose deprived (starvation) media for 24 h, and thereafter incubated with Carvedilol, Dexrazoxane, and mitoTempo 24 h at 37 °C. Next day, media was removed from wells, cells were carefully rinsed with PBS (2 × 200 μL), fresh media (200 μL) was added, and cells were incubated with Galuminox (20 μM) at 37 °C for 60 min. For controls, untreated cells were incubated with Galuminox (20 μM) under identical conditions. Thereafter, fluorescence images were acquired, and cellular uptake was quantified as described above.

2.4.4. Quantification of ROS in mouse lung cells

Quantitation of ROS post-LPS treatment was performed by using CellROX, a fluorogenic oxidative stress probe. CellROX is a cell-permeant dye and is weakly fluorescent in a reduced state. However, it exhibits bright green photostable fluorescence signal upon oxidation by reactive oxygen species (ROS) and subsequent binding to DNA, with absorption/emission maxima of 485/520 nm. Single cell lung suspensions were generated by cutting lung tissue into approximately 2 mm pieces and treatment with 0.5 mg/mL dispase (Sigma) and 5 units/mL of DNAse (Sigma) for 30 min at 37 °C and washed twice. Cell suspensions were filtered through a 70 micron filter and re-suspended at 200,000 cells per 500 μL of PBS and 5 μL of CellROX probe was added for 30 min at 37 °C. Cells were then analyzed for CellROX uptake by a FACS-SCAN flow cytometer (BD Biosciences, San Jose, CA).

2.5. Preclinical PET/CT imaging

All animal procedures were approved by the Washington University Animal Studies Committee. Imaging and biodistribution studies were performed in C57Bl6 mice (average weight, 24 g). Male mice (n = 4) were treated either with LPS at a dose of 5 μg/g or vehicle (saline) 24 h prior to imaging/biodistribution studies. For these studies, mice were anesthetized with isoflurane (2.0%) via an induction chamber and maintained with a nose cone. After anesthetization, the mice were secured in a supine position and placed in an acrylic imaging tray. Following intravenous tail-vein administration of ^{68}Ga-Galuminox (100 μL; 100 μCi; 2% ethanol in saline, 3.7 MBq), dynamic preclinical PET scans were performed over 60 min, using Inveon PET/CT scanner (Siemens Medical Solutions). PET data were stored in list mode, and reconstruction was performed using a 3D-OSEM method with detector efficiency, decay, dead time, attenuation, and scatter corrections applied. For anatomical visualization, PET images were also co-registered with CT images from an Inveon PET/CT scanner. ROIs were drawn over the lung, and standard uptake values (SUV) were calculated as the mean radioactivity per injected dose per animal weight.

2.6. Biodistribution studies (post preclinical imaging)

All animal procedures were approved by the Washington University Animal Studies Committee. Following microPET/CT imaging, mice (n = 4) were euthanized by cervical dislocation. Blood samples were obtained by cardiac puncture, organs then harvested rapidly, and all tissue samples analyzed for γ-activity using Beckman Gamma 8000 counter. All samples were decay-corrected to the time, the γ-counter was started. Standard samples were counted with the organs for each animal and represent 1% of the injected dose. An additional dose was diluted into milliQ water (100 mL) and aliquots (1 mL) were counted with each mouse. Data were quantified as the percentage injected dose (%ID) per gram of tissue (tissue kBq (injected kBq)$^{-1}$ (g tissue)$^{-1}$ x 100) Table S.2.

2.7. Lung histology and pulmonary edema studies

For wet to dry ratio the left lung mass was assessed before (wet) and after (dry) dehydration for 72 h at 65 °C. To measure airway protein bronchoalveolar lavage (3 × 1.0 ml saline extractions) was assayed for total protein content by absorbance at 595 nm (μQuant-Biotek) using a Bradford kit Protein Assay (BioRad) and bovine serum albumin as a standard (BSA), (Sigma). For histology, lung grafts were harvested, inflation fixed in formaldehyde, embedded in paraffin, sectioned, and stained with hematoxylin and eosin.

2.8. Statistical analysis

Statistical analysis were performed using unpaired Student's *t*-test using GraphPad Prism version 6.0 (GraphPad Software, San Diego, CA) or Excel 2016 (Microsoft, Redmond, WA). For all comparisons, $p < 0.05$ was considered statistically significant.

3. Results and discussion

Ga-LG-NOTA (which we now describe as Galuminox (**4**)), is a metalloprobe for the detection of total ROS. Galuminox was synthesized through reaction between LG-NOTA, the precursor ligand and $GaCl_3$ dissolved in dimethylsulfoxide (Fig. 2), purified, and analytically characterized. Proton NMR of Galuminox demonstrated a symmetrical coordination of the central gallium to the coordination core (N_3O_3) of the precursor ligand. Galuminox, when solubilized in PBS with 1.0% ethanol, and is excited with a 405 nm laser, it exhibits a broad emission peak between 450 and 540 nm with a maxima of 490 nm.

Integrated ROS comprise chemically reactive products of molecular oxygen (O_2) including the one-electron reduction product of molecular oxygen: superoxide ($O_2^{\cdot-}$). The superoxide can originate from numerous sources in vivo, including the mitochondrial electron transport chain and NADPH oxidase(s), which are activated under conditions of inflammation, ischemia, and tissue injury. Superoxide has also been shown to regulate distinct signaling cascades with specific molecular targets. Therefore, the ability to detect elevated ROS in patients could provide a better understanding of relationships between ROS, tissue injury, and disease staging. Furthermore, the ability to selectively identify specific ROS species may reveal critical information on signaling cascade that promote inflammation. Collectively, ROS

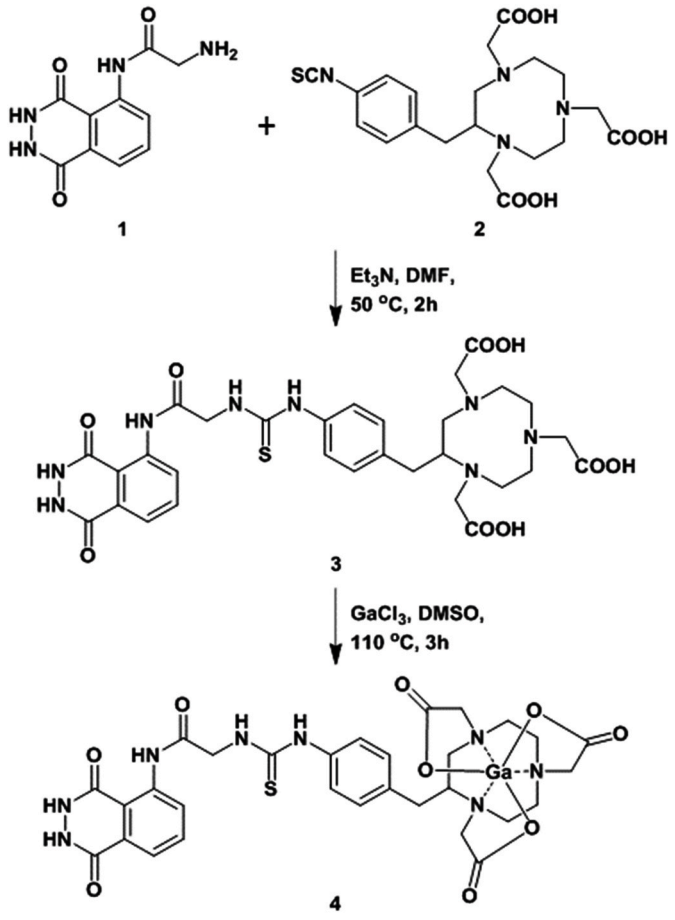

Fig. 2. Scheme for chemical synthesis of Galuminox.

processes involve formation of different reactive oxygen species. To measure ROS production, large number of methods have been developed, and are based upon detection by colorimetry, chemiluminescence, and fluorescence, depending on the probe used. While xanthine-xanthine oxidase (X-XO) and SIN-1 have been used for production of superoxide and nitric oxide (wherein the combination produces peroxynitrite) [55], respectively, the glucose-glucose oxidase (G-GO) system has been deployed for production of hydrogen peroxide [56]. Employing concentrations of Galuminox and X-XO, SIN-1, and G-GO *in vitro* conditions (Table S.1), we evaluated ability of Galuminox to detect different reactive oxygen species at 37 °C in PBS under physiological conditions (pH 7.2) and compared fluorescence output to that of untreated metalloprobe as a control using a fluorescence plate reader assay. The results are shown in Fig. 3. Galuminox showed ability to detect superoxide generated through either xanthine oxidase metabolism of xanthine or by thermal decomposition of SIN-1 in the presence of 2,4-carboxyphenyl-4,4–5,5-tetramethyl-imidazoline-1-oxyl-3-oxide (CPTIO), an inhibitor of nitric oxide. Under both conditions, oxidation of the probe was neutralized by the addition of superoxide dismutase (SOD) (Fig. 3). Furthermore, the metalloprobe showed ability to detect hydrogen peroxide produced during glucose oxidase catalyzed oxidation of glucose to gluconate. Under these conditions, the oxidation of the probe was mitigated in presence of catalase (CAT), which converts the hydrogen peroxide into carbon dioxide and water, thus indicating specificity of the probe to detect hydrogen peroxide (Fig. 3). Overall, the combined data indicate that Galuminox detects both superoxide and its downstream product, hydrogen peroxide.

Previously, we have shown that radiolabeled metalloprobes offer sensitive tools for evaluating quantitative accumulation of chemical entities within pooled cell populations. Although beneficial in translational nuclear imaging, this method precludes interrogation of pharmacological effects at a single cell level, within the same segment of cell population. Compared with radiotracer bioassays, fluorescence imaging offers a cost-efficient ionizing-radiation free technique to assess accumulation of metalloprobes at a single cell level, while beneficial in determining their intracellular localization under live cell conditions.

Lipopolysaccharide (LPS), also commonly known as endotoxin, is the major constituent of the outer cell wall of Gram-negative bacteria and is potent driver of ALI in septic patients [57]. LPS is detected by toll-like receptor 4 (TLR4), a broadly expressed pattern recognition receptor found both on leukocytes and nonhematopoietic cells. TLR4 engagement triggers the generation of mitochondrial superoxide from electron transport complex I, which in turn promotes bacterial killing [58]. To this end, we simultaneously assessed ROS production with the mitochondrial-superoxide probe MitoSOX [59,60] and Galuminox in the human lung alveolar epithelial carcinoma cell line A549 following LPS stimulation (Fig. 4A). When compared to untreated A549 control cells, LPS stimulation induced both higher fluorescence of MitoSOX and Galuminox, while and exhibiting a distinct pattern of probe co-localization, suggesting that Galuminox is taken up by superoxide-producing mitochondria (Fig. 4A). TLR4 engagement also induces the co-localization of ROS-generating mitochondria to low pH intracellular compartments such as phagolysosomes [58]. TLR4 engagement also leads to stimulation of autophagy in airway epithelial cells [61], which in turn can promote ROS production within lysosomes [62]. These literature precedents prompted us to ask if we could observe intracellular Galuminox activity within lysosomes. LPS stimulated A549 cells were co-stained with Galuminox and the pH sensitive fluorescent probe lysotracker (Fig. 4B). Galuminox demonstrated marked co-localization with lysotracker stained vesicles in LPS-treated A549 cells, indicating that Galuminox can detect ROS production also within lysosomes. Interestingly, mitochondria can produce ROS either within

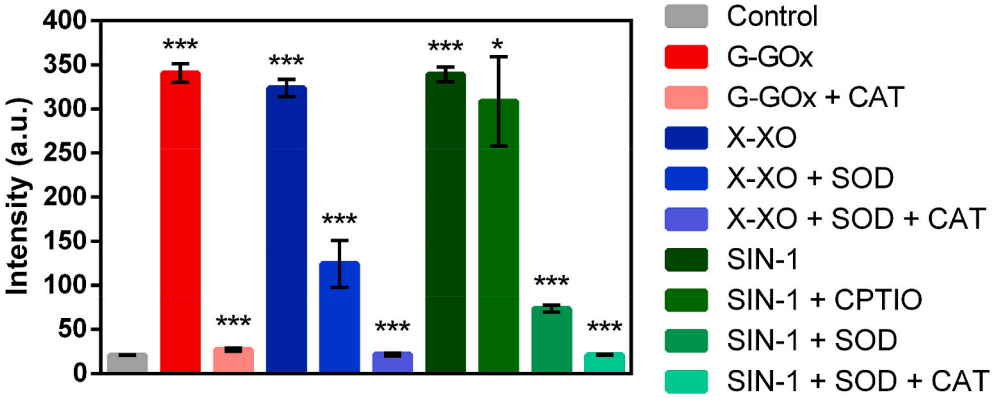

Fig. 3. Evaluation of Galuminox for detection of reactive oxygen species *in vitro*. Data are shown as mean fluorescence intensity (arbitrary units) ± SEM, where ***$p < 0.001$ and *$p < 0.4$ are determined by an unpaired student *t*-test.
Abbreviations: G: Glucose; GOx: Glucose oxidase; X: Xanthine; XO: Xanthine oxidase; SOD: Superoxide Dismutase; CAT: Catalase; SIN-1: 3-Morpholinylsydnoneimine chloride (SIN-1); and CPTIO: 2-(4-Carboxyphenyl)-4,4,5,5-tetramethylimidazoline-1-oxyl-3-oxide.

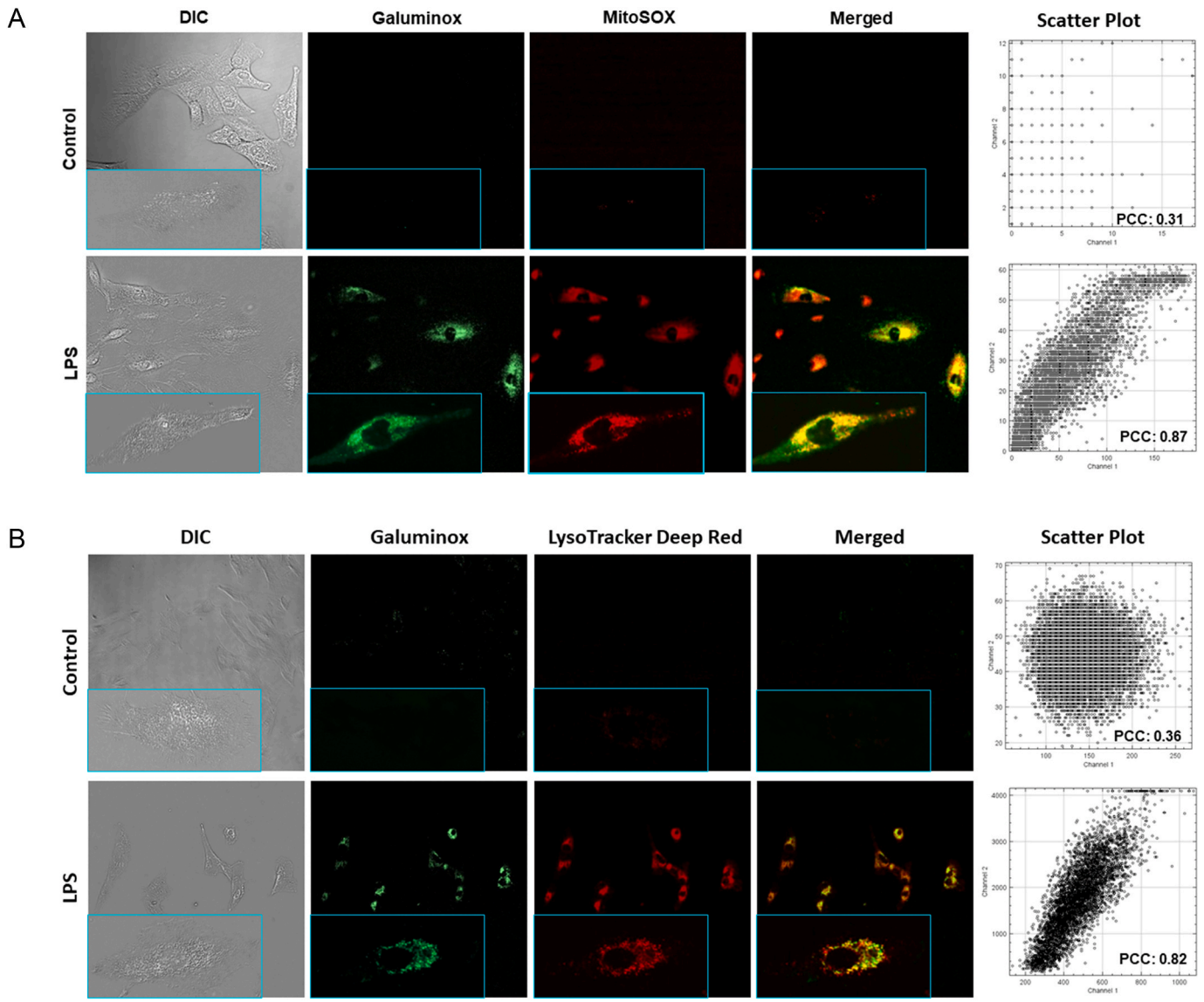

Fig. 4. Cellular accumulation of Galuminox in LPS-treated A549 cells and correlation with mitoSOX (A) and Lysotracker (B): Images were acquired using a 20× objective (all panels represent same magnification) in live human adenocarcinoma alveolar basal epithelial (A549) cells following incubation either in absence (control) or presence of LPS (1 μg/mL) for 24 h. Following treatment with LPS, A549 cells were incubated with Galuminox (20 μM) at 37 °C for 60 min either in the presence of MitoSOX (25 nM) or Lysotracker (1 μM). Shown is an uptake of Galuminox in A549 cells in reference to mitoSOX (ROS probe) and lysotracker (lysosome marker) under identical conditions. INSET (All Panels): Single Cell Image (Magnification: 60×).
Right: 4A and 4B. Scatter plots show relationships of spatial overlaps green (Galuminox) and red (mitoSox, **4A** or Lysotracker **4B**)) pixel intensities in A549 cells and their quantitative correlations using Pearson correlation coefficients (PCC). . (For interpretation of the references to color in this figure legend, the reader is referred to the Web version of this article.)

the cytoplasm or during autophagic removal and eventual sequestration within lysosomes-a process commonly referred to as mitophagy. Therefore, this aspect raises the possibility that Galuminox is measuring mitochondria ROS in one or both compartments. To answer this question explicitly, we utilized A549 cells that express mitochondrial targeted Keima (mt-Keima), a coral-derived acid-stable fluorescent protein that emits different-colored signals under acidic and neutral conditions. Notably, mt-Keima excitation peak shifts from 440 nm (under conditions of physiological pH in cytosol) to 586 nm (Lysosome pH: 4.0). Following LPS treatment of A549 cells that express mt-Keima, Galuminox shows a higher correlation with mt-Keima in the cytoplasm (440 nm, PCC: 0.86; Figure S2) than lysosome (564 nm; PCC: 0.55; Figure S2) for detection of ROS (Fig. 5). Given that we also observed that Galuminox co-localizes with MitoSOX-stained mitochondria (Fig. 4A), these data collectively suggest that Galuminox largely measures ROS production by mitochondria in the cytoplasm.

We next tested if mitigating mitochondrial oxidative stress through three different therapeutic strategies could be monitored by reductions in Galuminox activity. Carvedilol (CAR) is reported to reduce oxidative stress through inhibiting the mitochondrial exogenous nicotinamide adenine dinucleotide phosphate oxidase (NOX) activity [63]. Additionally, when CAR is co-administered with doxorubicin, an anticancer drug, reduces cell vacuolization in cardiomyocytes, preventing inhibition of mitochondrial respiration, thus mitigating doxorubicin induced reduction of Ca^{2+} loading [64]. Dexrazoxane (DEX) is an FDA approved drug for advanced breast cancer and functions by chelating free iron required for the catalytic function of mitochondrial NADH oxidase activity [65]. Finally, Mito-Tempo (MT) is mitochondria-targeted antioxidant that functions as a superoxide dismutase mimetic [66], and has been shown effective against experimental endotoxin-induced liver

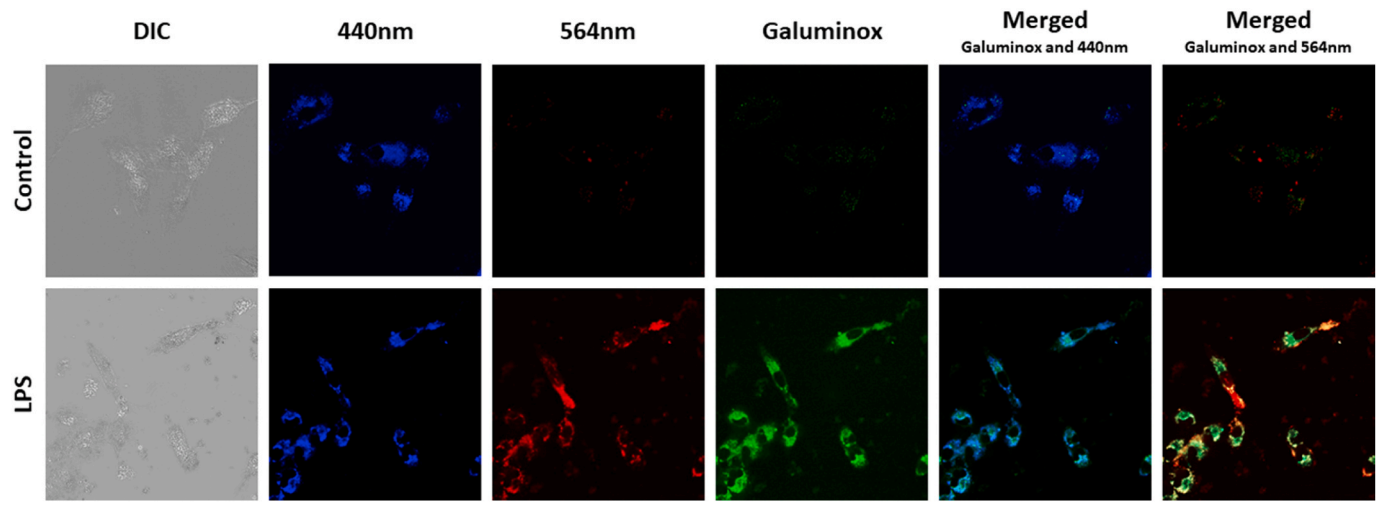

Fig. 5. Cellular accumulation of Galuminox in LPS-treated mt-Keima transfected A549 cells: Images were acquired using a 60× objective in live mt-Keima transfected A549 cells following incubation either in absence (control) or presence of LPS (1 μg/mL) for 24 h. Following treatment with LPS, mt-Keima transfected A549 cells were incubated with Galuminox (20 μM) at 37 °C for 60 min. **Top Panel**: Control; **Lower Panel**: LPS treated. Galuminox preferentially detects mitochondrial ROS (see merged image of Galuminox with Keima 440 nm) in the cytoplasm (see also scatter plot with Pearson correlation coefficients; Figure S.2).

injury and induction of mitochondrial NADH oxidase complex I superoxide activity in response to nutrient-deprivation-induced autophagy. For investigating the ability of Galuminox to measure therapeutic mitigation of ROS activity, in the presence or absence of CAR, DEX or Mito-Tempo, we treated A549 cells with LPS or nutrient-deprived A549 cells (by serum and glucose withdrawal) to induce ROS [67,68]. Twenty-four-hours (24 h)- post-LPS treatment or nutrient deprivation of A549 cells, we analyzed Galuminox uptake by live cell fluorescence imaging (Fig. 6). LPS-treated and nutrient deprived- A549 cells showed high retention of Galuminox in untreated (control) cultures. In contrast, however, probe uptake was significantly decreased in the presence of CAR, DEX, and Mito-Tempo when compared to control A549 cells. Some of these observations may also be explained by LPS-mediated mitochondrial depolarization or autophagic death, which can also lead to superoxide generation through the induction of mitochondrial intrinsic

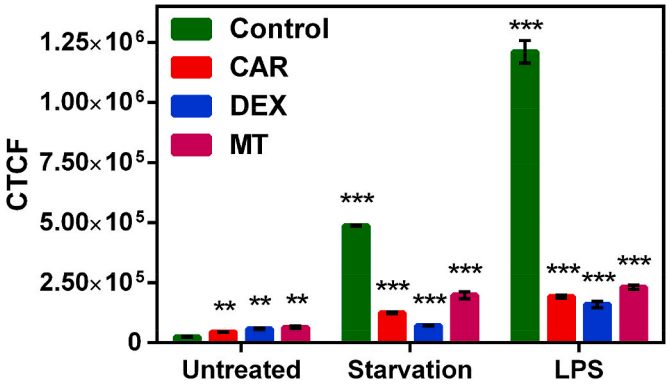

Fig. 6. Cellular accumulation of Galuminox either in serum and glucose deprived- or LPS-treated treated A549 cells either in presence or absence of Carvedilol (CAR), Dexrazoxane (DEX), and MitoTEMPO (MTT): Images were acquired using a 20× objective (all panels represent same magnification) in live human adenocarcinoma alveolar basal epithelial A549 cells. While A549 control cells were plated under normal conditions, both serum-and glucose-deprived (Starvation), and LPS treated cells were allowed to recover in presence of Carvedilol **(CAR),** Dexrazoxane **(DEX)**, and MitoTEMPO **(MTT)** for 48 h, and treated with Galuminox (20 μM) for 60 min, cell uptake was evaluated via live-cell imaging, and quantified as described earlier [50–52]. Corrected Total Cell Fluorescence (CTCF) = Integrated Density–(Area of selected cell X Mean fluorescence of background readings); (mean ± SEM), where ***p < 0.001 and **p < 0.01 are determined by an unpaired student *t*-test.

apoptosis [69], Taken together, these data show Galuminox potential to image ROS mitigating therapy in A549 cells.

For interrogating potential of Galuminox to serve as a ROS imaging probe in vivo, we utilized a well-established mouse model of LPS-mediated ALI [70]. In order to accomplish this objective, we prepared the PET mimetic, ^{68}Ga-Galuminox using a ligand exchange reaction. Preclinical PET/CT images at 1 h (summation of frames over 45min-60 min) post-administration of ^{68}Ga-Galuminox are shown in Fig. 7A. Pharmacokinetics were consistent with a dominant renal mode of probe excretion. Of note, ^{68}Ga-Galuminox demonstrated a 5-fold higher uptake in lungs of LPS-treated (Standard Uptake Value; SUV: 12.9 ± 1.85, n = 4) C57Bl6 mice compared with their saline (vehicle) only treated counterparts (SUV: 2.62 ± 0.48, n = 4) (Fig. 7B). Finally, SUV time-activity curves (TACs) showed consistently higher and stable retention of ^{68}Ga-Galuminox in lungs of LPS-treated mice (Fig. 7C) indicating retention of ^{68}Ga-Galuminox in the injured lung, thus enabling PET imaging of endotoxin mediated insult in vivo. For further correlating preclinical PET imaging data, post-imaging biodistribution studies were also conducted and percentage of activity remained in critical tissues at 1-h post injection of the radiotracer is shown in Fig. 8. ^{68}Ga-Galuminox demonstrated excretion profiles mediated by both hepatobiliary- and renal-modes of excretion. Compared with the saline-only treated mice (%ID/g: 39.7 ± 19.3), the radiotracer was retained 4-fold higher in lungs of LPS treated mice (%ID/g: 147.9 ± 25.8). The radiotracer also showed 1.4-fold higher retention in the blood of LPS treated mice (%ID/g: 3.96 ± 1.83) compared with their saline-treated counterparts ((%ID/g: 2.82 ± 0.88) Table S.2. The latter was consistent with expected LPS-induced activation of ROS within neutrophils. For assessing specific retention of the radiotracer within the lung tissue, the activity in the lung (4 folds) was normalized to that of blood (1.4 fold) for LPS treated mice and indicated 3 (4/1.4 = 2.85) fold higher specific retention in lungs of LPS treated mice (Table S.2). Additionally, LPS-induced effects were also observed in the liver (% ID/g: 10.5 ± 1.68 (LPS); 6.14 ± 0.66 (Saline); 1.7 fold) and bone (% ID/g: 2.14 ± 0.57 (LPS); 1.0 ± 0.34 (Saline); 2.1 fold) likely attributed to ROS mediated hepatotoxicity [71] and ROS upregulation in bone marrow macrophages [72], respectively, thus indicating systemic effect following administration of endotoxin.

To confirm pulmonary ROS generation in LPS-treated mice whole lung tissue was disrupted into single cell preparations and stained with CellROX Green, a well-established fluorescent probe that quantitates total ROS generation in live cells [73]. CellROX Green

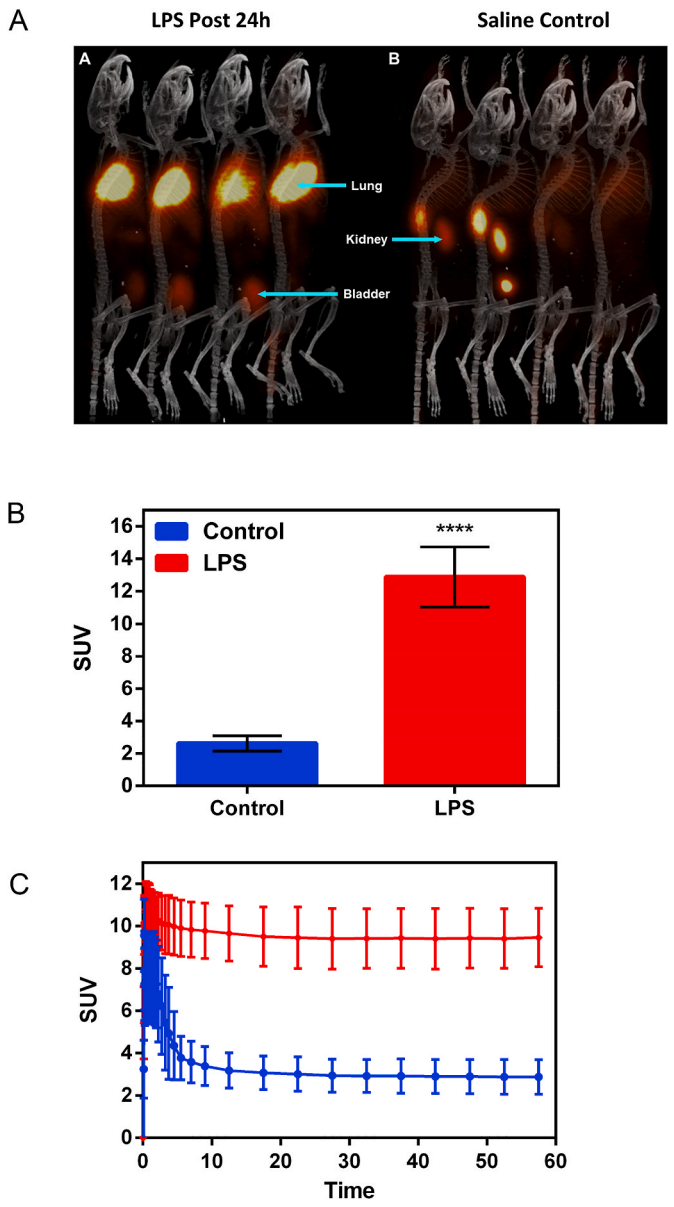

Fig. 7. Preclinical PET/CT Imaging. C57Bl6 mice (n = 4) were injected with either LPS or saline intraperitoneally. Following treatments, ^{68}Ga-Galuminox was injected via tail-vein into mice. **(A)** Dynamic PET images were acquired from 0 min to 60 min post tail-vein injection. PET/CT images as shown are a summation frames from 45 to 60 min. **Left Panel**: LPS (5 μg/g, 24 h post treatment); **Right Panel**: Saline-treated mice. **(B)** SUV analysis of ^{68}Ga-Galuminox uptake (mean ± SEM, where ****p < 0.0001 is determined by an unpaired student *t*-test) in lungs of Bl6 mice (n = 4) 24 h post either LPS- or saline treatments. **(C)** SUV Time-Activity Curve (TACs) of ^{68}Ga-Galuminox uptake in lungs of Bl6 mice 24 h post either LPS- or saline treatments indicating high and stable retention in lungs of LPS treated mice compared with their saline-treated counterparts.

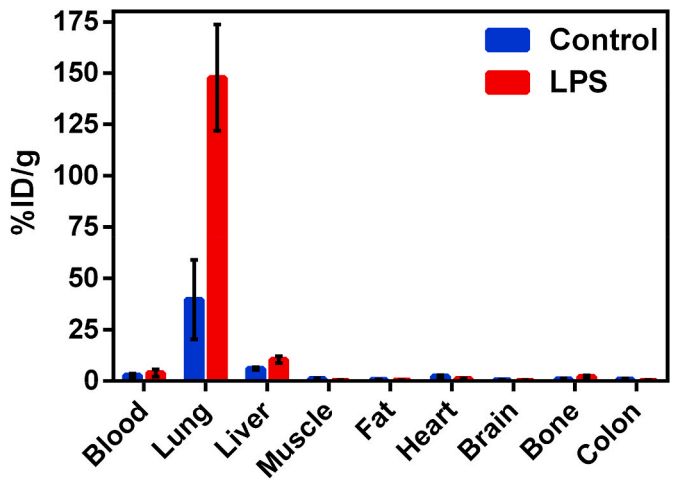

Fig. 8. Post-PET imaging biodistribution data (%ID/g) of Bl6 mice (24 h post-LPS treatment) and saline-treated controls.

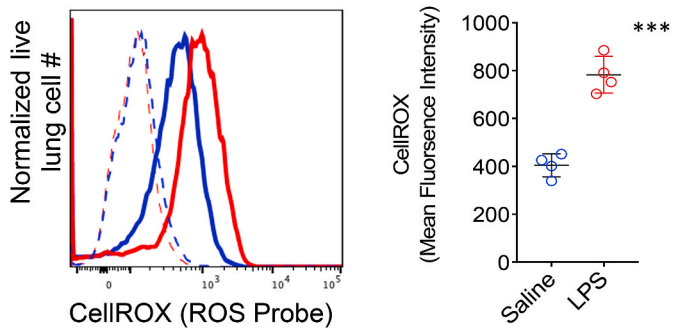

Fig. 9. Lung cell ROS generation measurement with CellROX. C57Bl6 mice (n = 4/group) were injected with either LPS or saline intraperitoneally and euthanized 24 post-treatment. A single cell lung suspension was stained with 5 μM of CellROX green for 30 min at room temperature and assessed for mean fluorescence intensity (MFI) by flow cytometric analysis (FACS). FACS histogram plot (left) are representative measurements from saline (blue) and LPS (red) treated mice where dotted lines show background MFI (unstained) and solid lines show CellROX probed mice. Scatter plot on the right show MFI measurements for individual mice along with a group mean MFI ±SEM where ***p < 0.001 as determined by an unpaired student *t*-test. (For interpretation of the references to color in this figure legend, the reader is referred to the Web version of this article.)

(absorption/emission maxima of ~485/520 nm) is a cell-permeant weakly fluorescent dye in a reduced state and exhibits a bright green photostable fluorescence following oxidation by ROS and subsequent trapping within intracellular compartments. Lung cells were quantified for CellROX oxidation by measuring the mean fluorescence emission intensity (MFI) of between 515 and 545 nm following excitation with a 488 nm laser using a flow cytometer. We observed approximately a two-fold higher ROS activity in lung cells of LPS treated mice when compared to their counterparts that received saline as a vehicle (Fig. 9). ROS injures lung tissue by disrupting hemostatic barriers that lead to pulmonary edema through breaking down endothelial cell tight junctions and triggering epithelial cell necrosis [74,75]. Therefore, we asked if Galuminox uptake was associated with histological and physiological evidence of acute injury. Hemotoxylin and Eosin staining of lungs of LPS-treated mice revealed polynuclear infiltration and thickening of the alveolar epithelial membranes (Fig. 10A). Analysis of lung tissue wet to dry ratio and bronchioalveolar lavage protein content, both measures of pulmonary edema, were both significantly elevated in LPS-treated mice (Fig. 10B & C). Taken collectively, these data indicate that Galuminox uptake is a measure of ROS generation following ALI.

4. Conclusions

Given that overproduction of ROS or insufficient elimination thereof has been associated with numerous diseases, such as diabetes, heart failure, cancer, and ARDS, including lung transplant failures, molecular imaging agents capable of detecting superoxide production and other downstream ROS in vivo would offer versatile tools to study role of ROS in normal physiology and pathophysiology of chronic diseases. To this

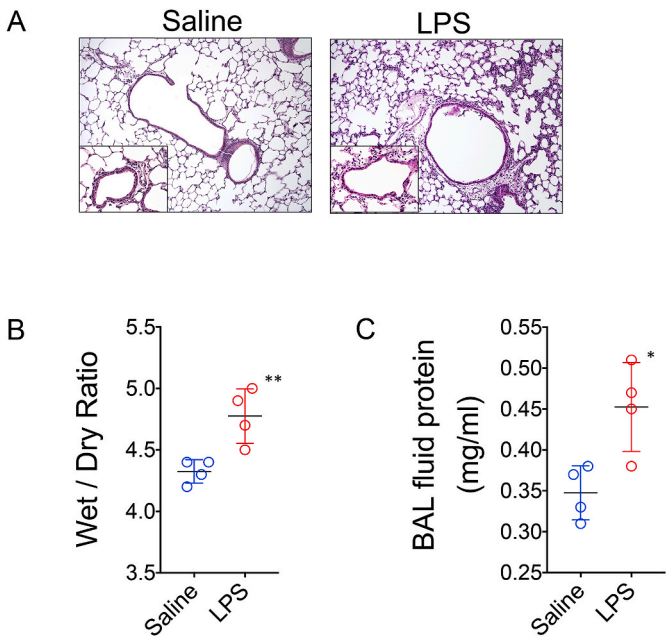

Fig. 10. LPS mediated acute lung injury. C57Bl6 mice (n = 4/group) were injected with either LPS or saline intraperitoneally and euthanized 24 post-treatment. (**A**) H&E lung histology (100X and 400X inset) from a representative mouse from each group. (**B**) Lung wet to dry ratio and (**C**) BAL fluid protein content shown for individual mice and as a mean ± SEM where $^{**}p < 0.01$ and $^{*}p < 0.05$ as determined by an unpaired student *t*-test.

end, the current study shows that ^{68}Ga-Galuminox, a PET radiotracer (incorporated with Ga-68, a generator-produced radionuclide for widespread availability of the technology) can be synthesized in high yield and high radiochemical purity in approx. 30 min for preclinical imaging. Our data also show that Galuminox is a molecular imaging probe of superoxide and downstream ROS products both *in vitro*. Overall, the PET probe demonstrates high sensitivity to visualize LPS-induced inflammation within lungs thus offering a template scaffold for further validations in ROS models of chronic diseases in vivo. Collectively, both preclinical imaging and ex vivo data reinforce our observations that ^{68}Ga-Galuminox PET imaging could provide a noninvasive diagnosis for ROS mediated acute lung injury and investigating role of ROS in pathophysiology of other chronic conditions in vivo.

Declaration of competing interest

The authors declare no conflict of interest.

Acknowledgements

This study was supported in part by grants R01HL111163, RO1HL142297 (VS); NIBIB P41 EB025815 (RG); U24CA209837 (KIS) and R01HL094601, P01AI116501 (AG) from the National Institutes of Health and Mallinckrodt Institute of Radiology (MIR) departmental funds for imaging studies. The funding agencies had no role in study design, data collection and analysis, decision to publish, or preparation of the manuscript. Authors thank the Preclinical Imaging Facility at MIR for help in performing PET/CT imaging studies. The Preclinical Imaging Facility is supported by the Siteman Cancer Center Support Grant (P30CA091842).

Appendix A. Supplementary data

Supplementary data to this article can be found online at https://doi.org/10.1016/j.redox.2020.101690.

References

[1] U. Raaz, et al., Hemodynamic regulation of reactive oxygen species: implications for vascular diseases, Antioxidants Redox Signal. 20 (2014) 914–928.
[2] P.D. Ray, B.W. Huang, Y. Tsuji, Reactive oxygen species (ROS) homeostasis and redox regulation in cellular signaling, Cell. Signal. 24 (2012) 981–990.
[3] J. Roy, J.M. Galano, T. Durand, J.Y. Le Guennec, J.C. Lee, Physiological role of reactive oxygen species as promoters of natural defenses, Faseb. J. 31 (2017) 3729–3745.
[4] S.K. Powers, L.L. Ji, A.N. Kavazis, M.J. Jackson, Reactive oxygen species: impact on skeletal muscle, Comp. Physiol. 1 (2011) 941–969.
[5] D.I. Brown, K.K. Griendling, Regulation of signal transduction by reactive oxygen species in the cardiovascular system, Circ. Res. 116 (2015) 531–549.
[6] S.J. Forrester, D.S. Kikuchi, M.S. Hernandes, Q. Xu, K.K. Griendling, Reactive oxygen species in metabolic and inflammatory signaling, Circ. Res. 122 (2018) 877–902.
[7] H. Cui, Y. Kong, H. Zhang, Oxidative stress, mitochondrial dysfunction, and aging, J Signal Transduct 2012 (2012) 646354.
[8] T. Finkel, Signal transduction by reactive oxygen species, J. Cell Biol. 194 (2011) 7–15.
[9] M.D. Evans, M. Dizdaroglu, M.S. Cooke, Oxidative DNA damage and disease: induction, repair and significance, Mutat. Res. 567 (2004) 1–61.
[10] D. Moris, et al., The role of reactive oxygen species in the pathophysiology of cardiovascular diseases and the clinical significance of myocardial redox, Ann. Transl. Med. 5 (2017) 326.
[11] C.M.O. Volpe, P.H. Villar-Delfino, P.M.F. Dos Anjos, J.A. Nogueira-Machado, Cellular death, reactive oxygen species (ROS) and diabetic complications, Cell Death Dis. 9 (2018) 119.
[12] A.J. Kattoor, N.V.K. Pothineni, D. Palagiri, J.L. Mehta, Oxidative stress in atherosclerosis, Curr. Atherosclerosis Rep. 19 (2017) 42.
[13] M. Jesenak, M. Zelieskova, E. Babusikova, Oxidative stress and bronchial asthma in children-causes or consequences? Front Pediatr 5 (2017) 162.
[14] F. Cioffi, R.H.I. Adam, K. Broersen, Molecular mechanisms and genetics of oxidative stress in alzheimer's disease, J. Alzheim. Dis. : JAD 72 (2019) 981–1017.
[15] I. Khmaladze, K.S. Nandakumar, R. Holmdahl, Reactive oxygen species in psoriasis and psoriasis arthritis: relevance to human disease, Int. Arch. Allergy Immunol. 166 (2015) 135–149.
[16] L.J.S. da Fonseca, V. Nunes-Souza, M.O.F. Goulart, L.A. Rabelo, Oxidative stress in rheumatoid arthritis: what the future might hold regarding novel biomarkers and add-on therapies, Oxidative medicine and cellular longevity 2019 (2019) 7536805.
[17] P. Davalli, T. Mitic, A. Caporali, A. Lauriola, D.R.O.S. D'Arca, Cell senescence, and novel molecular mechanisms in aging and age-related diseases, Oxidative medicine and cellular longevity 2016 (2016) 3565127.
[18] M. Kellner, et al., ROS signaling in the pathogenesis of acute lung injury (ALI) and acute respiratory distress syndrome (ARDS), Adv. Exp. Med. Biol. 967 (2017) 105–137.
[19] Z. Dong, Y. Yuan, Accelerated inflammation and oxidative stress induced by LPS in acute lung injury: iotanhibition by ST1926, Int. J. Mol. Med. 41 (2018) 3405–3421.
[20] M. Singer, et al., The third international consensus definitions for sepsis and septic shock (Sepsis-3), J. Am. Med. Assoc. 315 (2016) 801–810.
[21] G.R. Bernard, et al., The American-European Consensus Conference on ARDS. Definitions, mechanisms, relevant outcomes, and clinical trial coordination, Am. J. Respir. Crit. Care Med. 149 (1994) 818–824.
[22] G.D. Rubenfeld, E. Caldwell, J. Granton, L.D. Hudson, M.A. Matthay, Interobserver variability in applying a radiographic definition for ARDS, Chest 116 (1999) 1347–1353.
[23] L.R. Goodman, Congestive heart failure and adult respiratory distress syndrome. New insights using computed tomography, Radiol. Clin. 34 (1996) 33–46.
[24] L. Gattinoni, et al., Adult respiratory distress syndrome profiles by computed tomography, J. Thorac. Imag. 1 (1986) 25–30.
[25] P. Pelosi, S. Crotti, L. Brazzi, L. Gattinoni, Computed tomography in adult respiratory distress syndrome: what has it taught us? Eur. Respir. J. 9 (1996) 1055–1062.
[26] D. Chiumello, et al., Global and regional diagnostic accuracy of lung ultrasound compared to CT in patients with acute respiratory distress syndrome, Crit. Care Med. 47 (2019) 1599–1606.
[27] X. Chen, X. Tian, I. Shin, J. Yoon, Fluorescent and luminescent probes for detection of reactive oxygen and nitrogen species, Chem. Soc. Rev. 40 (2011) 4783–4804.
[28] B.C. Dickinson, C. Huynh, C.J. Chang, A palette of fluorescent probes with varying emission colors for imaging hydrogen peroxide signaling in living cells, J. Am. Chem. Soc. 132 (2010) 5906–5915.
[29] B.C. Dickinson, Y. Tang, Z. Chang, C.J. Chang, A nuclear-localized fluorescent hydrogen peroxide probe for monitoring sirtuin-mediated oxidative stress responses in vivo, Chem. Biol. 18 (2011) 943–948.
[30] N. Karton-Lifshin, et al., A unique paradigm for a Turn-ON near-infrared cyanine-based probe: noninvasive intravital optical imaging of hydrogen peroxide, J. Am. Chem. Soc. 133 (2011) 10960–10965.
[31] F. Si, Y. Liu, K. Yan, W. Zhong, A mitochondrion targeting fluorescent probe for imaging of intracellular superoxide radicals, Chem. Commun. 51 (2015) 7931–7934.
[32] G.C. Van de Bittner, E.A. Dubikovskaya, C.R. Bertozzi, C.J. Chang, In vivo imaging of hydrogen peroxide production in a murine tumor model with a chemoselective bioluminescent reporter, Proc. Natl. Acad. Sci. U.S.A. 107 (2010) 21316–21321.
[33] A. Agarwal, S.S. Allamaneni, T.M. Said, Chemiluminescence technique for measuring reactive oxygen species, Reprod. Biomed. Online 9 (2004) 466–468.

[34] W. Chu, et al., Development of a PET radiotracer for non-invasive imaging of the reactive oxygen species, superoxide, in vivo, Org. Biomol. Chem. 12 (2014) 4421–4431.
[35] N.E. Boutagy, et al., In vivo reactive oxygen species detection with a novel positron emission tomography tracer, (18)F-DHMT, allows for early detection of anthracycline-induced cardiotoxicity in rodents, JACC Basic Transl Sci 3 (2018) 378–390.
[36] A.A. Wilson, et al., Evaluation of a novel radiotracer for positron emission tomography imaging of reactive oxygen species in the central nervous system, Nucl. Med. Biol. 53 (2017) 14–20.
[37] V. Carroll, et al., A boronate-caged [(1)(8)F]FLT probe for hydrogen peroxide detection using positron emission tomography, J. Am. Chem. Soc. 136 (2014) 14742–14745.
[38] S. Al-Karmi, et al., Preparation of an (18) F-Labeled hydrocyanine dye as a multimodal probe for reactive oxygen species, Chemistry 23 (2017) 254–258.
[39] P. Sadiku, et al., Prolyl hydroxylase 2 inactivation enhances glycogen storage and promotes excessive neutrophilic responses, J. Clin. Invest. 127 (2017) 3407–3420.
[40] F.C. Liu, et al., A novel NOX2 inhibitor attenuates human neutrophil oxidative stress and ameliorates inflammatory arthritis in mice, Redox Biol 26 (2019) 101273.
[41] P.A. Kramer, S. Ravi, B. Chacko, M.S. Johnson, V.M. Darley-Usmar, A review of the mitochondrial and glycolytic metabolism in human platelets and leukocytes: implications for their use as bioenergetic biomarkers, Redox Biol 2 (2014) 206–210.
[42] H.A. Jones, et al., In vivo measurement of neutrophil activity in experimental lung inflammation, Am. J. Respir. Crit. Care Med. 149 (1994) 1635–1639.
[43] R.L. Melcher, B.M. Moerschbacher, An improved microtiter plate assay to monitor the oxidative burst in monocot and dicot plant cell suspension cultures, Plant Methods 12 (2016) 5.
[44] C. Dodeigne, L. Thunus, R. Lejeune, Chemiluminescence as diagnostic tool. A review, Talanta 51 (2000) 415–439.
[45] T.I. Quickenden, C.P. Ennis, J.I. Creamer, The forensic use of luminol chemiluminescence to detect traces of blood inside motor vehicles, Luminescence 19 (2004) 271–277.
[46] B.A. Stoica, et al., Improving luminol blood detection in forensics, J. Forensic Sci. 61 (2016) 1331–1336.
[47] S. Bedouhene, F. Moulti-Mati, M. Hurtado-Nedelec, P.M. Dang, J. El-Benna, Luminol-amplified chemiluminescence detects mainly superoxide anion produced by human neutrophils, Am J Blood Res 7 (2017) 41–48.
[48] D. Mueller, et al., Radiolabeling of DOTA-like conjugated peptides with generator-produced (68)Ga and using NaCl-based cationic elution method, Nat. Protoc. 11 (2016) 1057–1066.
[49] N. Sun, et al., A fluorescence-based imaging method to measure in vitro and in vivo mitophagy using mt-Keima, Nat. Protoc. 12 (2017) 1576–1587.
[50] J. Sivapackiam, et al., 68Ga-Galmydar: a PET imaging tracer for noninvasive detection of Doxorubicin-induced cardiotoxicity, PloS One 14 (2019), e0215579.
[51] G. Sundaram, K. Binz, V. Sharma, M. Yeung, V. Sharma, Live-Cell Fluorescence Imaging: assessment of Thioflavin T uptake profiles in human epidermal carcinoma cells, Med Chem Commun 9 (2018) 946–950.
[52] B. Jakic, M. Buszko, G. Cappellano, G. Wick, Elevated sodium leads to the increased expression of HSP60 and induces apoptosis in HUVECs, PloS One 12 (2017), e0179383.
[53] W. Stauffer, H. Sheng, H.N. EzColocalization Lim, An ImageJ plugin for visualizing and measuring colocalization in cells and organisms, Sci. Rep. 8 (2018) 15764.
[54] K.W. Dunn, M.M. Kamocka, J.H. McDonald, A practical guide to evaluating colocalization in biological microscopy, Am. J. Physiol. Cell Physiol. 300 (2011) C723–C742.
[55] M. Ishii, S. Shimizu, K. Momose, T. Yamamoto, SIN-1-induced cytotoxicity in cultured endothelial cells involves reactive oxygen species and nitric oxide: protective effect of sepiapterin, J. Cardiovasc. Pharmacol. 33 (1999) 295–300.
[56] Z. Tao, R.A. Raffel, A.K. Souid, J. Goodisman, Kinetic studies on enzyme-catalyzed reactions: oxidation of glucose, decomposition of hydrogen peroxide and their combination, Biophys. J. 96 (2009) 2977–2988.
[57] B. Beutler, E.T. Rietschel, Innate immune sensing and its roots: the story of endotoxin, Nat. Rev. Immunol. 3 (2003) 169–176.
[58] A.P. West, et al., TLR signalling augments macrophage bactericidal activity through mitochondrial ROS, Nature 472 (2011) 476–480.
[59] M.E. Kauffman, et al., MitoSOX-based flow cytometry for detecting mitochondrial ROS, React Oxyg Species (Apex) 2 (2016) 361–370.
[60] B.M. Polster, D.G. Nicholls, S.X. Ge, B.A. Roelofs, Use of potentiometric fluorophores in the measurement of mitochondrial reactive oxygen species, Methods Enzymol. 547 (2014) 225–250.
[61] X.H. Wang, et al., Lipopolysaccharide induces autophagy by targeting the AMPK-mTOR pathway in human nasal epithelial cells, Biomed. Pharmacother. 96 (2017) 899–904.
[62] C. Kubota, et al., Constitutive reactive oxygen species generation from autophagosome/lysosome in neuronal oxidative toxicity, J. Biol. Chem. 285 (2010) 667–674.
[63] P.J. Oliveira, D.J. Santos, A.J. Moreno, Carvedilol inhibits the exogenous NADH dehydrogenase in rat heart mitochondria, Arch. Biochem. Biophys. 374 (2000) 279–285.
[64] P.J. Oliveira, et al., Carvedilol-mediated antioxidant protection against doxorubicin-induced cardiac mitochondrial toxicity, Toxicol. Appl. Pharmacol. 200 (2004) 159–168.
[65] D. Lebrecht, et al., Dexrazoxane prevents doxorubicin-induced long-term cardiotoxicity and protects myocardial mitochondria from genetic and functional lesions in rats, Br. J. Pharmacol. 151 (2007) 771–778.
[66] J.N. Peoples, A. Saraf, N. Ghazal, T.T. Pham, J.Q. Kwong, Mitochondrial dysfunction and oxidative stress in heart disease, Exp. Mol. Med. 51 (2019) 1–13.
[67] P. Marambio, et al., Glucose deprivation causes oxidative stress and stimulates aggresome formation and autophagy in cultured cardiac myocytes, Biochim. Biophys. Acta 1802 (2010) 509–518.
[68] S. Rodic, M.D. Vincent, Reactive oxygen species (ROS) are a key determinant of cancer's metabolic phenotype, Int. J. Canc. 142 (2018) 440–448.
[69] C.Y. Chuang, et al., Lipopolysaccharide induces apoptotic insults to human alveolar epithelial A549 cells through reactive oxygen species-mediated activation of an intrinsic mitochondrion-dependent pathway, Arch. Toxicol. 85 (2011) 209–218.
[70] G. Matute-Bello, C.W. Frevert, T.R. Martin, Animal models of acute lung injury, Am. J. Physiol. Lung Cell Mol. Physiol. 295 (2008) L379–L399.
[71] Y. Zhao, et al., Protective effect of suberoylanilide hydroxamic acid against lipopolysaccharide-induced liver damage in rodents, J. Surg. Res. 194 (2015) 544–550.
[72] O.J. Sul, H.J. Park, H.J. Son, H.S. Choi, Lipopolysaccharide (LPS)-Induced autophagy is responsible for enhanced osteoclastogenesis, Mol. Cell. 40 (2017) 880–887.
[73] J.J. Grailer, et al., Critical role for the NLRP3 inflammasome during acute lung injury, J. Immunol. 192 (2014) 5974–5983.
[74] R. Herrero, G. Sanchez, J.A. Lorente, New insights into the mechanisms of pulmonary edema in acute lung injury, Ann. Transl. Med. 6 (2018) 32.
[75] R.L. Zemans, S.P. Colgan, G.P. Downey, Transepithelial migration of neutrophils: mechanisms and implications for acute lung injury, Am. J. Respir. Cell Mol. Biol. 40 (2009) 519–535.